Received: 11 July 2025 | Revised: 9 September 2025 | Accepted: 23 September 2025 | Published online: 13 October 2025

RESEARCH ARTICLE

Smart Wearable Technology
2025, Vol. 00(00) 1–12
DOI: 10.47852/bonviewSWT52026773

BON VIEW PUBLISHING

An Android-Based Embedded Modified Iterative Fusion Deep Neural Network for Automated Detection of Macular Diseases Using OCT Images

Umar Shafiq Ahmad[1] and Rajesh Kumar Tripathy[1,*]

[1]*Department of Electronics and Electrical Engineering, Birla Institute of Technology and Science, India*

Abstract: Retinal optical coherence tomography (OCT) is a noninvasive and high-resolution diagnostic imaging modality used for early detection of choroidal neovascularization (CNV), diabetic macular edema (DME), and drusen-based macular diseases (MDs). The manual procedure for screening these MDs using OCT images is cumbersome and may result in a false diagnosis. Hence, there is a requirement for an artificial intelligence-enabled automated approach for the accurate detection of macular disorders. This paper presents a modified iterative fusion deep neural network (MIFDNN) model and its implementation on an Android framework for the automated detection of CNV, DME, and drusen using OCT images. Initially, the U-Net model is used to obtain the enhanced OCT image from the noisy OCT image. The enhanced OCT image is used as input for the proposed MIFDNN model for detecting MDs. The MIFDNN employs a sophisticated dual-branch architecture comprising a custom basic branch deep convolutional neural network (CNN) module for hierarchical feature extraction, a fusion branch for iterative multiscale feature integration, dense layers, and a softmax layer for detecting MDs. The basic branch deep CNN consists of five convolution layers, five batch normalization (BN) layers, and three max-pooling layers. The classification performance of the proposed MIFDNN model is evaluated using OCT images from a public dataset. Our model has achieved a remarkable average classification accuracy of 98.17% using a 3-fold cross-validation strategy, outperforming several existing methods to detect MDs using OCT images. To facilitate real-world application, we have performed post-training quantization to reduce the size of the proposed MIFDNN model. The quantized model is successfully deployed on an Android platform, where the on-device inference maintained an impressive 98% accuracy with a throughput of approximately 92 images per minute, validating the proposed model's practical feasibility for screening MDs using OCT images.

Keywords: OCT image, MDs, MIFDNN model, U-Net denoising, quantization, Android deployment

1. Introduction

The retinal diseases are the leading cause of vision loss in the world [1]. The macular diseases (MDs) are a subset of retinal diseases that affect the small central area of the retina called the macula, which is responsible for sensing light and sending visual signals to the brain [2]. The early diagnosis and effective treatment of these MDs are essential to prevent vision loss for human perception and overall quality of life. The MDs, such as diabetic macular edema (DME), choroidal neovascularization (CNV), drusen, and other forms of macular degeneration, can lead to partial or complete vision loss if not detected in the early stage [2]. CNV is characterized by the formation of abnormal blood vessels under the retina [3]. These vessels are prone to leakage and bleeding, often leading to scarring and rapid deterioration of central vision. Similarly, the DME occurs as a complication of diabetic retinopathy (DR) and involves the accumulation of extracellular fluid in the macula due to vascular leakage [4]. Drusens are extracellular deposits composed primarily of lipids and proteins, located between the retinal pigment epithelium and Bruch's membrane [5]. The small drusen can be benign, but the presence of larger or numerous drusen is an early indicator of age-related macular degeneration. Optical coherence tomography (OCT) is a noninvasive imaging modality that captures high-resolution cross-sectional images of the retina of the eye [6]. It allows ophthalmologists to visualize retinal structures in detail and is an essential tool in diagnosing various macular disorders [6]. The manual interpretation of OCT scans for diagnosing MDs is a tedious and expertise-dependent process that often requires trained and experienced ophthalmologists to evaluate subtle anatomical differences across multiple cross-sectional slices [7]. The recent advancements in artificial intelligence (AI) have enabled the development of automated diagnostic systems capable of analyzing medical images and providing diagnostic decisions that are comparable to those of expert clinicians [8]. The AI-based approaches are mainly implemented on cloud-based systems, which suffer from healthcare data privacy concerns and high latency and are dependent on stable internet connectivity for automated detection of different diseases using medical images [9]. In healthcare engineering, edge computing provides automated and real-time diagnostic decisions closer to the data recording or imaging system in medical centers without transmitting the patient's data

*Corresponding author: Rajesh Kumar Tripathy, Department of Electronics and Electrical Engineering, Birla Institute of Technology and Science, India. Email: tripathyrk@hyderabad.bits-pilani.ac.in

to the cloud. The Android-based edge device facilitates cost-effective, user-friendly, privacy-preserving, and real-time analysis of medical images without the requirement of cloud connectivity [9]. Therefore, the development of novel AI-based approaches and their implementation on Android devices is interesting for automated and real-time detection of MDs using OCT images. Different AI-based techniques have been proposed in the last decade for the automated detection of MDs using OCT images [10]. Srinivasan et al. [11] have computed the histogram of oriented gradients (HOG) features from OCT images and utilized the support vector machine (SVM)-based machine learning (ML) classifier for detecting MDs. Similarly, different ML-based methods coupled with various types of features extracted from OCT images have been employed for detecting MDs [12, 13]. In Das et al. [7], the authors have utilized the VGG16-based transfer learning model [14] for classifying healthy versus CNV versus DME versus drusen classes using OCT images. The same authors have also utilized an InceptionV3-based model for classifying MDs using OCT images [7, 15]. Fang et al. [16] have suggested an iterative fusion-based convolutional neural network (IFCNN) for detecting MDs using OCT images. They have used the VGG16 model in the basic branch of IFCNN for detecting MDs. Huang et al. [17] have proposed a layer-guided CNN-based deep learning (DL) model for automated detection of CNV, DME, and drusen-based MDs using OCT images. Das et al. [2] have employed the multiscale spatial pyramid decomposition of OCT images and a CNN at each scale, followed by feature fusion for automated detection of MDs. Mishra et al. [18] have suggested a composite attention-based DL model to detect MDs using OCT images. Akça et al. [19] have used different versions of vision transformer (ViT)-based DL models for detecting MDs such as DME, CNV, and drusen using OCT images. In Jaimes et al. [20], the authors have used the VGG16-based transfer learning network to detect MDs using OCT images. Similarly, Bhandari et al. [21] have proposed a lightweight CNN model architecture for detecting MDs using OCT images. The ML-based methods depend on the use of image processing techniques to extract a fixed set of features, the use of optimization and ranking-based techniques for selection of features, and accurate selection of the parameters of the classifiers for detecting MDs using OCT images [11–13]. The DL models have shown higher classification results than ML-based methods for detecting MDs using OCT images. However, these existing DL-based methods are based on cloud-based inference and have not been implemented on edge devices for detecting MDs using OCT images. Edge computing for health care is based on deploying the AI model on embedded devices, smartphones, and tablets for on-device detection of different diseases [22]. The techniques, such as quantization and pruning, are used to reduce the size of the DL model for deploying it into embedded devices [9]. The novelty of this work lies in the development of a new DL model and its implementation on an Android device for real-time detection of MDs using OCT images. The salient contributions of this work are as follows:

1) A modified iterative fusion-based deep neural network (MIFDNN) model architecture is proposed for detecting MDs using OCT images.
2) The post-training quantization (PTQ) of the MIFDNN models using reduced precision-based representation of weight parameters with 16-bit floating point (FP16), 16-bit integer (INT16), and 8-bit integer (INT8) is performed.
3) The deployment of the reduced precision-based MIFDNN model on an Android device for real-time detection of MDs such as CNV, DME, and drusen using OCT images. The remaining sections of this paper are organized as follows.

In Section 2, a detailed description of the OCT image dataset used in the proposed work is provided. The proposed method is described in Section 3. The results obtained based on the evaluation of the proposed method and the discussion of these results are presented in Section 4. Finally, the conclusions of this work are written in Section 5.

2. OCT Images Dataset

This study uses a publicly available retinal OCT dataset [23, 24] for developing and evaluating the proposed DL model to detect MDs. The dataset comprises a total of 84,495 grayscale OCT B-scan images, collected from 4686 patients at the Shiley Eye Institute, University of California, San Diego [24]. All scans have been obtained using the Heidelberg Spectralis OCT system, which is known for its high axial resolution and consistent image acquisition quality [24]. The dataset contains the OCT images for four classes: CNV (37,455 images), DME (11,598 images), drusen (8866 images), and healthy (26,565 images). We have used the total number of OCT images (84,484) for this work to develop and evaluate the proposed MIFDNN model for detecting MDs. The 11-OCT image difference between the stated (84,495) and actual (84,484) dataset size appears to be a minor discrepancy in the original dataset documentation, which we have verified through direct file counting. An independent dataset (second dataset) is also used to verify the effectiveness of the proposed method in a cross-dataset-based scenario (method trained using one dataset and tested using another dataset containing OCT images) for detecting MDs. The second dataset consists of 24000 OCT images and has 8 classes (healthy, DME, CNV, drusen, central serous retinopathy, DR, macular hole) [25]. The OCT images for the training set, validation set, and test set are given as 18400, 2800, and 2800, respectively, in the second dataset. In this work, we have used a total of 1750 OCT images (350 OCT images for each class) from healthy, DME, CNV, and drusen classes to evaluate the performance of the proposed method for detecting MDs. The OCT images in the datasets are of different sizes. We have resized each OCT image in both datasets to a size of $224 \times 224 \times 1$.

3. Proposed Method

The proposed method for detecting MDs using OCT images is represented in a block diagram as depicted in Figure 1. The approach consists of the denoising of the OCT image and the MIFDNN model architecture for detecting MDs.

3.1. OCT image denoising

In this work, we have used the U-Net model [26] for the denoising of OCT images. For the U-Net model, 400 OCT images from each of the four classes (CNV, DME, drusen, and normal) are selected for generating masks for the training. This mask generation is based on the use of different image processing operations, such as the extraction of retinal layers, the removal of whitening background, aspect-ratio-preserving square cropping, image sharpening, and patch-based noise elimination and region filling using erosion and dilation methods [27, 28]. After generating the masks, the U-Net model is trained to obtain an enhanced OCT image. The "Adam" optimizer, "binary cross entropy" as cost function, the number of epochs as 32, batch size as 8, and 20% of the training OCT images as validation data are utilized for the training of the U-Net model. The enhanced OCT image is evaluated using the trained U-Net model with the input as the test OCT images. The performance of the U-Net model is

Figure 1
Block diagram representation of the proposed approach for detecting MDs using OCT images

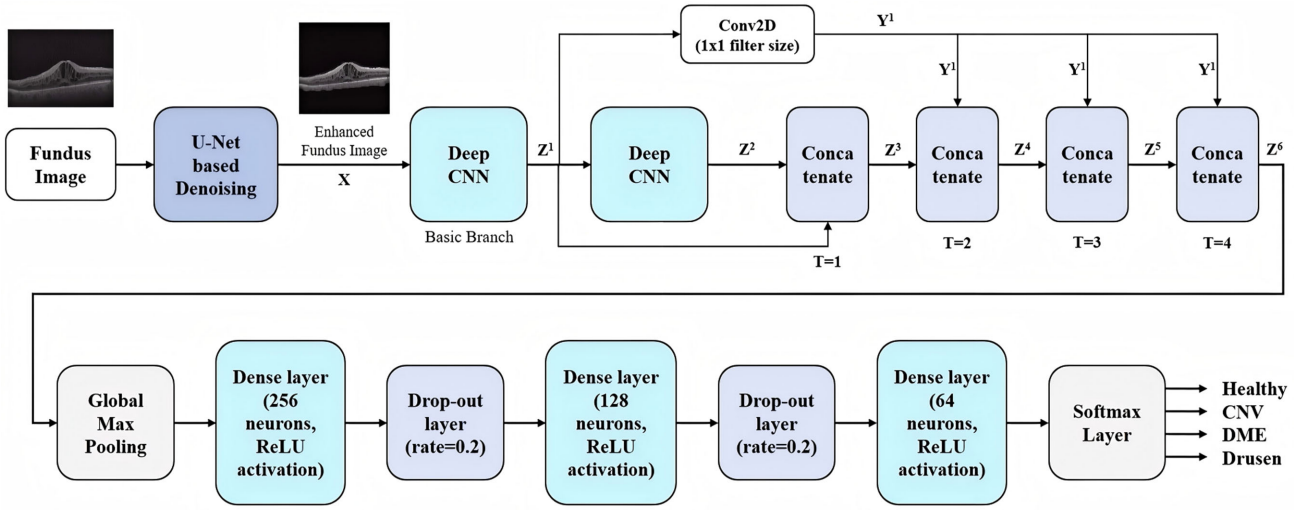

evaluated using measures such as macro intersection over union (IoU), macro dice coefficient (DC), weighted IoU, and weighted DC [29]. The original OCT image and the enhanced OCT image are shown in Figure 2(a) and (b), respectively. It is observed that the U-Net model effectively segments the retinal layers and enhances the diagnostic quality of the OCT image by reducing the noise and detecting the boundaries. After evaluating the enhanced OCT image, the proposed MIFDNN model is implemented for detecting MDs.

3.2. MIFDNN model

The overall architecture of the MIFDNN model is shown in Figure 1. The proposed MIFDNN model consists of a basic branch for hierarchical feature extraction and a fusion branch for iterative multi-layer feature integration for classifying OCT images. This dual-path strategy in the MIFDNN model enables the network to capture both fine structural nuances and high-level abstractions in the OCT images [16], which are critical when differentiating between visually similar conditions such as CNV and DME classes. The basic branch of the MIFDNN model is constructed as a deep CNN, which is shown in Figure 3. It begins with a 2D convolutional layer using a kernel size of 3 × 3 with 32 filters, followed by BN and a 2 × 2 max-pooling layer. This is followed by a second convolutional layer with a kernel size of 5 × 5 and 64 filters, again succeeded by BN and max-pooling layers. A third convolutional block, with a 5 × 5 kernel and 128 filters, is added next and is followed by a fourth convolutional layer with a 3 × 3 kernel and 384 filters. Finally, a fifth convolutional layer with a 3 × 3 kernel and 128 filters is included before the final max-pooling layer. For the 2D convolution layer, the feature map computed in the l^{th} layer is given as follows [30]:

$$Z_f^l(i,j) = \sum_{c=1}^{C}\sum_{m=1}^{M}\sum_{n=1}^{N} Z_c^{l-1}(i.s+m, j.s+n)K_c^f(m,n) + b^f \quad (1)$$

where $Z_f^l(i,j)$ is the output feature map for l^{th} layer, $Z_f^{l-1}(i,j)$ is the input feature map at l^{th} layer, f and c are the indices for output and input channels, and $K_c^f(m,n)$ and b^f are the kernel matrix and bias value for the f^{th} output feature map or channel. s corresponds to the stride along both horizontal and vertical directions of the input feature map. Similarly, for the l^{th} max-pooling layer, the feature map is calculated for the f^{th} channel, and it is given as follows [30]:

Figure 2
(a) Raw OCT image. (b) Enhanced OCT image evaluated using the U-Net-based denoising technique

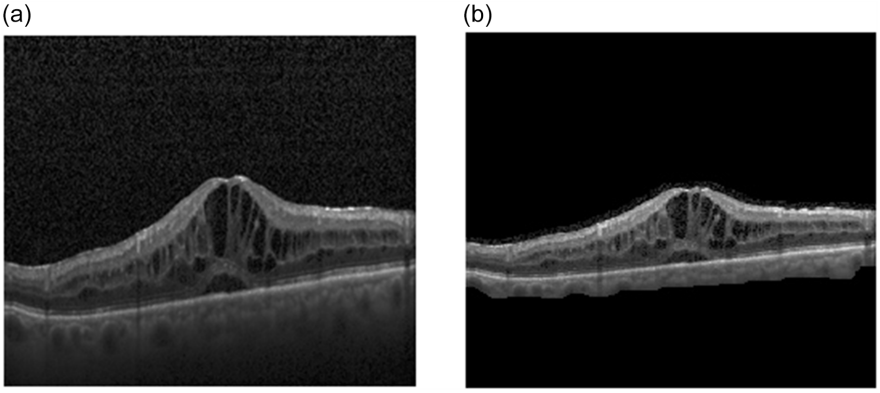

Figure 3
Architecture of the deep CNN used in the proposed MIFDNN model

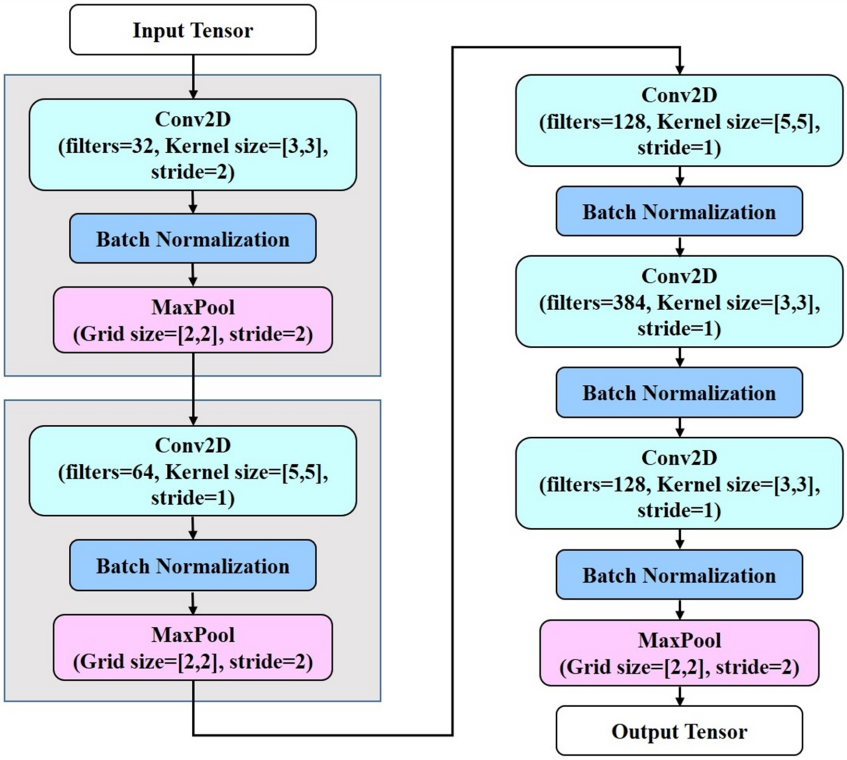

$$Z_f^l(i,j) = \underset{\substack{1 \le m \le M \\ 1 \le n \le N}}{max} Z_f^{l-1}(i.s+m, j.s+n) \quad (2)$$

In the concatenation branch of the proposed MIFDNN model, the features extracted from the basic branch (deep CNN model) are concatenated to generate the merged features. At the end of the fusion or concatenation branch, we have used a global max-pooling layer to reduce spatial dimensions. After the max-pooling layer, a fully connected block comprising three dense layers is added. The first dense layer consists of 256 units with ReLU activation and L_2-norm regularization, after which a dropout layer with a 20% rate is applied to prevent overfitting. This is followed by a second dense layer with 128 units, also regularized using the L_2-norm of the weight matrix, and followed by another dropout layer. A third dense layer with 64 units is then added, again incorporating L_2-norm regularization of the weight matrix. Finally, a dense output layer with 4 units is used, corresponding to the four OCT classes (healthy, CNV, DME, and drusen), and employs a softmax activation function to generate class probabilities. The training, validation, and test instances of the MIFDNN model are selected using hold-out validation with a split percentage of 70%, 10%, and 20%, respectively. We have also considered the stratified 3-fold cross-validation (CV) technique to train and validate the proposed MIFDNN model. For the training of the MIFDNN model, the RMSprop optimizer with a learning rate of 0.0001 is considered.

The OCT dataset exhibited significant class imbalance across the four classes: CNV (37455 OCT images, 44.5%), normal (26565 OCT images, 31.6%), DME (11598 OCT images, 13.8%), and drusen (8866 OCT images, 10.5%). This imbalance ratio of approximately 4.2:1 between the majority (CNV) and minority (drusen) classes can cause a substantial risk for the proposed MIFDNN model to be biased toward the CNV class. In this work, we have evaluated the class weight for i^{th} class as follows [31]:

$$w_i = \frac{m}{(C \times m_i)} \quad (3)$$

where m and m_i are the total number of samples and the number of samples in the i^{th} class, respectively. The computed class weights for CNV, healthy, DME, and drusen classes are 0.56, 0.79, 1.81, and 2.37, respectively. In this work, we have considered the weighted sparse categorical cross-entropy (WSCC) loss function for the MIFDNN model. The WSCC loss function is given as follows [31]:

$$WSCC = \frac{1}{B}\sum_{i=1}^{B} w_i\{-\log(p_{i,y_i})\}, \quad (4)$$

where p_{i,y_i} is the predicted probability of the ith corrected class. The weights penalize misclassifications of underrepresented classes (drusen, DME) more heavily while reducing the influence of overrepresented classes (CNV) during training. To mitigate overfitting and dynamically adapt the learning process, we have integrated two key callbacks during training, such as Reduce learning rate on plateau to decrease the learning rate and early stopping to allow training of the MIFDNN model to halt early while restoring the model weights that yielded the lowest validation loss. The MIFDNN model is trained for up to 32 epochs per fold, using a batch size of 16, and class weights are applied to address the class imbalance issues. Furthermore, we have also considered the 5-fold CV for evaluating the classification performance of the MIFDNN model to detect MDs using OCT images. To assess the proposed MIFDNN model's performance on unseen OCT images, a separate test dataset comprising 968 OCT images (242 OCT images per class) is utilized. The classification metrics, such as accuracy, F1-score, precision,

and recall, are used for evaluating the performance of the MIFDNN model to detect MDs [32].

3.3. Quantization and Android-based deployment

In this work, the trained MIFDNN model is converted into the TensorFlow Lite format, which is optimized for on-device inference. To enable efficient deployment of the MIFDNN model on resource-constrained environments such as mobile and edge devices, we have applied PTQ using TensorFlow's optimization tools [33]. PTQ works by reducing the numerical precision of model parameters and activations, typically converting from 32-bit floating point (FP32) to lower-precision formats like FP16, INT16, and INT8, which significantly minimizes both memory footprint and computational cost during inference [9]. To enable real-world applicability of the proposed system, the final trained models are deployed on an Android mobile platform using Android Studio and Java [9, 22]. We have deployed both the U-Net-based denoising model and the MIFDNN model for preparing the Android application for real-time OCT image denoising and detection of MDs. The core components in the Android app's user interface (UI) are image acquisition, image display, and prediction of results. The image acquisition part in the app has two action buttons (one button has the option "Take picture" and the other "select from gallery"). The image display part shows the enhanced OCT image. Similarly, after pressing the prediction of result button, the class label corresponding to the OCT image is shown. The TensorFlow Lite versions of U-Net-based denoising and MIFDNN models are kept in the backend of the Android app. The Android app's UI is simple and requires uploading or taking a picture of an OCT image to obtain the class label for detecting MDs. The device used for the deployment of the proposed approach is a Realme RMX3388 smartphone containing a MediaTek Dimensity 810 octa-core processor and 6GB of random access memory (RAM). The smartphone runs on a ColorOS 13-based Android 13 operating system. The TensorFlow Lite Support Library v0.1.0 runtime has been used for executing the proposed model for detecting MDs using OCT images. All computations are performed using a central processing unit only, and no graphics processing unit has been used in this work.

4. Results and Discussion

The performance of different quantized versions of the U-Net model for the denoising and segmentation of OCT images is depicted in Table 1. It is observed that the FP16 version of the U-Net model has demonstrated better denoising and segmentation performance with the highest IoU and dice scores as compared to other quantized versions of U-Net models. The hold-out validation results for detecting MDs using the proposed MIFDNN model for different quantization cases using enhanced OCT images are depicted in Table 2. It is observed that the accuracy value of the MIFDNN model with the INT8-based quantization case is obtained as 91.05%, which is slightly higher compared to the MIFDNN models using FP32 (90.88%), FP16 (90.48%), and INT16 (90.71%) cases for the detection of MDs. Additionally, the Kappa score of the INT8-based model is found to be 0.8669, which also slightly outperforms the FP16 (0.8592), FP32 (0.8650), and INT16 (0.8625) quantized versions. These results indicate the potential of INT8 quantization in maintaining robust performance while reducing model complexity and inference cost. The results obtained from evaluating the trained proposed MIFDNN model on the independent test set are presented in Table 3. In this case, the accuracy, precision, recall, and Kappa values are identical for the FP32, FP16, and INT16 quantization cases, each achieving an accuracy of 97.93%, precision of 97.99%, recall of 97.93%, and a Kappa score of 0.9724. However, for the INT8-based model, there is a slight drop in the performance metrics, with the accuracy reduced to 97.42%, precision to 97.51%, recall to 96.67%, and the Kappa score to 0.9651. The reductions observed for the INT8 case are 0.51% in accuracy, 0.48% in precision, 1.26% in recall, and 0.0073 in Kappa score compared to the other quantization versions. Despite this marginal decline, the INT8 model maintains competitive performance, reinforcing its viability for deployment in resource-constrained environments. The per-class receiver operating characteristics (ROC) curves of the proposed MIFDNN model using OCT images from the independent test set are depicted in Figure 4. The area under the curve (AUC) values are close to one for all four classes, indicating the robustness and discrimination ability of the proposed MIFDNN model for detecting MDs using OCT images. We have also shown the per-class and overall AUC values of MIFDNN models in Table 4 for different quantization cases using OCT images from the independent test set for detecting MDs using OCT images. It is observed that the FP32, FP16, and INT16 versions of the MIFDNN models achieve identical macro- and micro-average AUCs and per-class AUCs, indicating minimal impact of quantization for detecting MDs. The INT8 version of the MIFDNN model shows a slight reduction in macro- and micro-average AUCs compared to other quantization versions. However, the per-class AUC is still higher than 0.99, confirming robust discriminative performance even under the reduced precision-based representation of the MIFDNN model for detecting MDs using OCT images.

Table 1
Results of the U-Net model for different quantization cases for obtaining enhanced OCT images

Quantization	Macro IoU (%)	Macro Dice (%)	Weighted IoU (%)	Weighted Dice (%)
FP32	96.55	98.24	96.55	98.24
FP16	96.75	98.34	96.75	98.34
INT16	96.55	98.24	96.55	98.24
INT8	96.35	98.14	96.35	98.14

Table 2
Hold-out validation results of the MIFDNN model for detecting MDs using OCT images

Quantization	Accuracy (%)	Precision (%)	Recall (%)	Kappa
FP32	90.88	87.29	87.78	0.865
FP16	90.48	86.72	87.42	0.8592
INT16	90.71	87.11	87.58	0.8625
INT8	91.05	87.89	87.29	0.8669

Table 3
Results obtained for MIFDNN model using the OCT images from an independent test set for detecting MDs

Quantization	Accuracy (%)	Precision (%)	Recall (%)	Kappa
FP32	97.93	97.99	97.93	0.9724
FP16	97.93	97.99	97.93	0.9724
INT16	97.93	97.99	97.93	0.9724
INT8	97.42	97.51	96.67	0.9651

Figure 4
Per-class ROC curves of the MIFDNN model to detect MDs using the OCT images from an independent test set

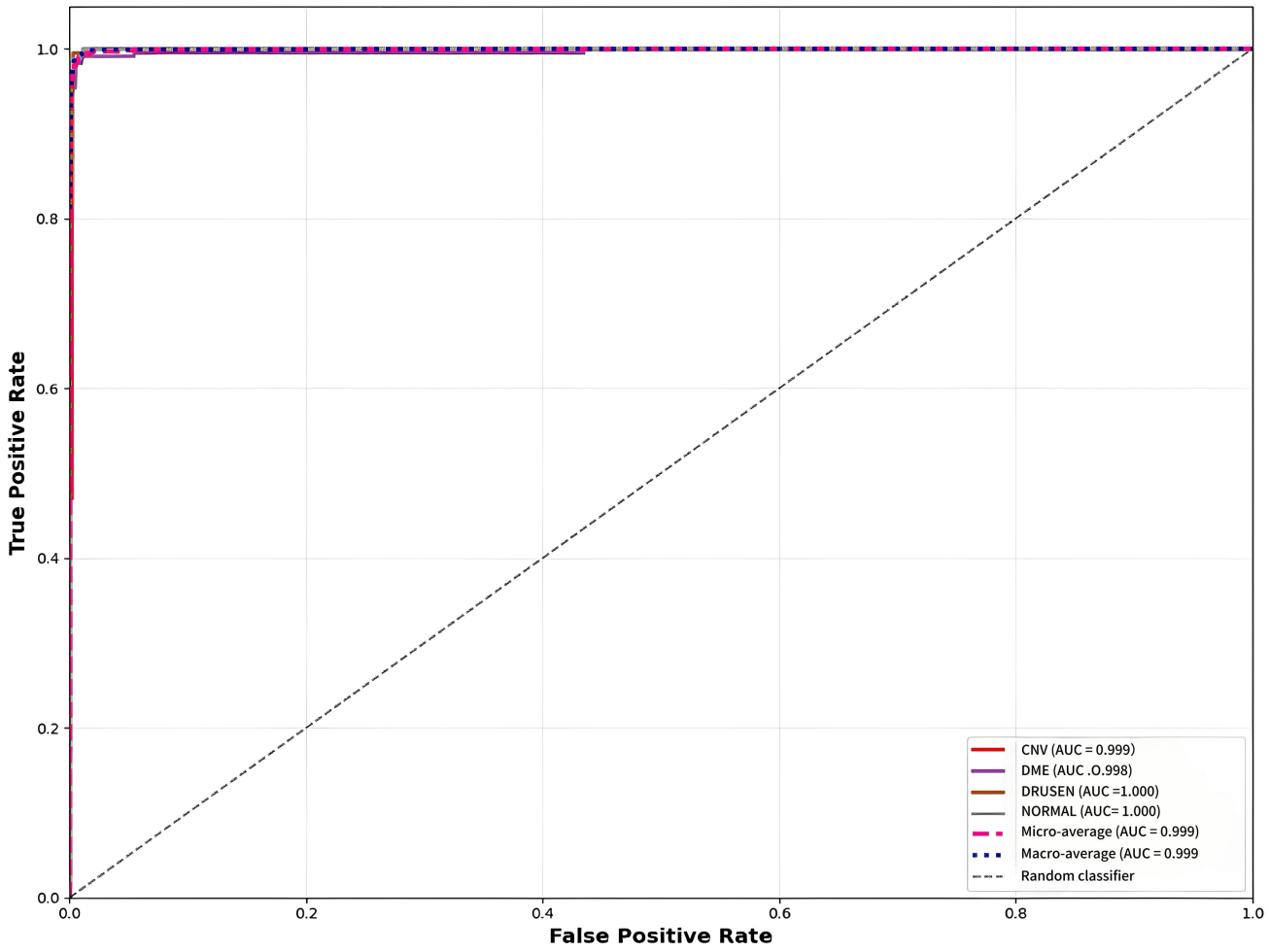

Table 4
Per-class and overall AUC values of MIFDNN models for different quantization cases to detect MDs using the OCT images from an independent test set

Quantization	Macro-Average AUC	Micro-Average AUC	AUC for CNV class	AUC for DME class	AUC for Drusen class	AUC for Healthy class
FP32	0.999	0.999	0.999	0.998	1	1
FP16	0.999	0.999	0.999	0.998	1	1
INT16	0.999	0.999	0.999	0.998	1	1
INT8	0.995	0.995	0.993	0.997	0.996	0.996

Further evaluation of the proposed MIFDNN model is conducted using CV to assess the consistency and generalization capability of the model across varying data splits. The results obtained using a 5-fold CV approach on the independent test set are illustrated in Table 5. The performance metrics for FP32, FP16, and INT16 cases are found to be identical, demonstrating the robustness of the MIFDNN model across different numerical representations. For the MIFDNN model with INT8-based quantized version case, the average accuracy, average precision, and average recall values are obtained as above 96% for detecting MDs using OCT images. This uniformity in results across quantization levels reflects the MIFDNN model's stable learning behavior under different computational conditions. To further strengthen the reliability of the model, experiments are repeated using a 3-fold CV strategy, and the results are presented in Table 6. In this scenario, the FP32, FP16, and INT16 quantized MIFDNN models again demonstrated identical performance, reaching a high average accuracy of 98.17%, precision of 98.17%, recall of 98.17%, and an impressive Kappa score of 0.9757. The INT8 quantized MIFDNN model, while slightly lower, still maintained excellent results with an accuracy of 98.14%, precision of 98.19%, recall of 98.14%, and a Kappa score of 0.9752. The accuracy drop in the INT8 case is marginal, just 0.03% in accuracy, 0.03% in recall, and 0.0005 in Kappa, yet it remains a

Table 5
Classification performance of the MIFDNN model for detecting MDs using enhanced OCT images using 5-fold CV

Quantization	Accuracy (%)	Precision (%)	Recall (%)	Kappa
FP32	96.43 ± 0.50	96.44 ± 0.50	96.43 ± 0.50	0.9523 ± 0.0067
FP16	96.43 ± 0.50	96.44 ± 0.50	96.43 ± 0.50	0.9523 ± 0.0067
INT16	96.43 ± 0.50	96.44 ± 0.50	96.43 ± 0.50	0.9523 ± 0.0067
INT8	96.40 ± 0.52	96.41 ± 0.52	96.40 ± 0.52	0.9510 ± 0.0070

Table 6
Classification performance of the MIFDNN model for detecting MDs using enhanced OCT images using 3-fold CV

Quantization	Accuracy (%)	Precision (%)	Recall (%)	Kappa	95% CI
FP32	98.17 ±0.10	98.21 ± 0.10	98.17 ± 0.10	0.9757 ±0.0013	(97.80–98.90)
FP16	98.17 ± 0.10	98.21 ± 0.10	98.17 ± 0.10	0.9757 ± 0.0013	(97.80–98.90)
INT16	98.17 ± 0.10	98.21 ± 0.10	98.17 ± 0.10	0.9757 ±0.0013	(97.80–98.90)
INT8	98.14 ± 0.10	98.19 ± 0.10	98.14 ± 0.10	0.9752 ± 0.0013	(97.80–98.90)

Table 7
Classification performance of the proposed method based on the removal of the basic branch module and fusion module from MIFDNN to detect MDs using OCT images

Model selected	Accuracy (%)	Precision (%)	Recall (%)	Kappa
No fusion module in MIFDNN	96.07	96.24	96.07	0.94
No basic branch module in MIFDNN	86.5	87.2	86.5	0.8533
MIFDNN (basic branch and fusion modules included)	98.35	98.38	98.35	0.978

strong contender for low-resource deployment scenarios. In a 3-fold CV, each validation fold includes 33.33% of the data (OCT images) for testing, while in a 5-fold CV, each validation fold includes only 20% of the data. With stratification, the 3-fold splits happened to be slightly more balanced and representative of the overall dataset distribution, which helped the MIFDNN model achieve higher classification performance for detecting MDs using enhanced OCT images. The statistical significance of the differences in the accuracy values between quantization schemes of the proposed MIFDNN model is assessed using bootstrap confidence intervals (n = 1000 bootstrap samples, and 95% confidence level (CI)) [34]. Given the identical performance metrics for FP32, FP16, and INT16 quantization (98.35% accuracy), these schemes show no statistically meaningful differences. For INT8 quantization, a 0.03% reduction in accuracy falls within the typical measurement uncertainty for the MIFDNN models on the test OCT images to detect MDs. The magnitude of this difference is substantially smaller than the standard error typically associated with neural network evaluation, suggesting the difference may not be statistically significant. The identical performance across FP32, FP16, and INT16 quantization indicates that these compression techniques preserve model accuracy for detecting MDs using OCT images. The MIFDNN model with INT8 quantization case shows minimal performance impact that is likely within normal evaluation variance.

We have evaluated the classification results of the MIFDNN model in two cases: case 1 (removing the basic branch deep CNN module only from MIFDNN) and case 2 (removing only the fusion module from MIFDNN), as shown in Table 7. It is observed that the model implemented using no fusion module in MIFDNN has demonstrated an accuracy value of 96.07%, which is lower than the MIFDNN with both basic and fusion branches for detecting MDs using OCT images. Similarly, the model based on MIFDNN with no basic deep CNN branch has produced an overall accuracy value of 86.50% for detecting MDs. In the proposed MIFDNN model, the hierarchical feature extraction and multiscale feature integration help to extract discriminative features from OCT images. Due to this reason, the proposed MIFDNN has obtained higher accuracy in detecting MDs using OCT images. In Table 8, we have shown the classification results of the proposed MIFDNN model using the OCT images of an independent dataset. It is observed that, for the cross-dataset scenario, the MIFDNN model has obtained an accuracy value of 95.71% to detect MDs using OCT images. A 0.57% drop in accuracy value is observed when the INT8-based quantization of the MIFDNN model is considered, compared to that of the FP32, FP16, and INT16-based versions of the MIFDNN model for detecting MDs. We have conducted McNemar's test [35] on the predictions of the MIFDNN model pairwise across quantization formats (FP32 versus FP16, FP32 versus INT16, FP16 versus INT16) using the OCT images independent test set for detecting MDs using OCT images. For FP32 versus FP16, FP32 versus INT16, and FP16 versus INT16 cases of the proposed MIFDNN models, the p-values evaluated from McNemar's test are found as $p = 1.0$ for all three cases. These results demonstrate that there are

Table 8
Results of the MIFDNN model evaluated using OCT images from an independent dataset in the testing phase for different quantization cases to detect MDs

Quantization	Accuracy (%)	Precision (%)	Recall (%)	Kappa
FP32	95.71	95.75	95.71	0.9428
FP16	95.71	95.75	95.71	0.9428
INT16	95.71	95.75	95.71	0.9428
INT8	95.57	95.61	95.57	0.9409

Figure 5
t-SNE plot evaluated using the learned feature vectors at the last dense layer of the MIFDNN model using OCT images from the independent test set

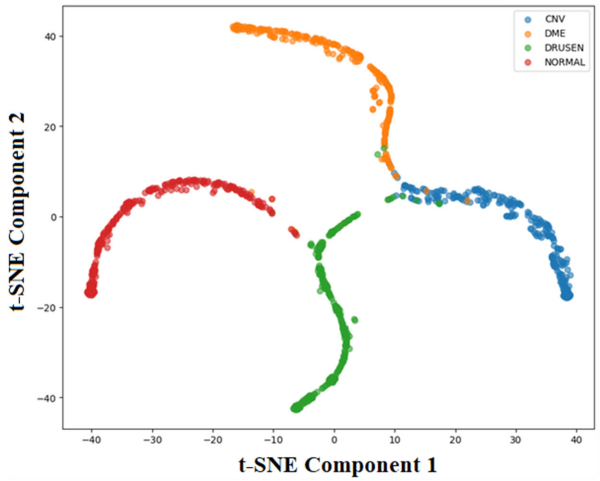

no statistically significant differences in predictive performance among FP32, FP16, and INT16 versions of the proposed MIFDNN models using OCT images from an independent test dataset for detecting MDs. This supports our claim that quantization preserves the accuracy of the proposed MIFDNN model without degradation, while reducing memory or computation requirements.

To interpret the decision-making capability of the proposed MIFDNN model, two types of visualizations are employed. Figure 5 presents the t-distributed Stochastic Neighbor Embedding (t-SNE) plot generated using the learned feature vectors from the final dense layer of the proposed MIFDNN model using the OCT images from the independent test set. The clear separation between clusters corresponding to the four Retinal diseases classes – normal, CNV, DME, and drusen – demonstrates that the model is effectively learning discriminative features for each category. In Figure 6, we have shown the gradient-weighted class activation mapping (Grad-CAM) plots to highlight the important regions for the detection of MDs using the proposed MIFDNN model with input as an OCT image for each class. These plots or heatmaps emphasize the specific retinal regions the MIFDNN model attends to when making predictions, providing visual confirmation of the proposed MIFDNN model's focus on clinically relevant locations for each disease class. Figure 7 depicts the MIFDNN model's predictions for each of the four classes (normal, CNV, DME, and drusen) as seen on the mobile phone screen. For validation, the Android application is tested using a set of 100 OCT images per class, totaling 400 test samples. Out of these, the model correctly classified 394 images, resulting in an overall accuracy of 98.50%. This high performance confirms the MIFDNN model's consistency and effectiveness in real-time settings, making it suitable for point-of-care diagnostics and portable medical support. The proposed MIFDNN model on an Android device has 1 misclassification instance between CNV and DME classes, 2 between DME and CNV classes, and 1 between drusen and CNV classes. This misclassification occurs due to the similarity between the morphologies of the OCT images of the two classes. It is also observed that 1 OCT image of the DME class is predicted as normal, and 1 OCT image of the normal class is predicted as the drusen class by the MIFDNN model on an Android device.

The details regarding the sizes, parameters, and giga floating point operations per second (GFLOPS) of the MIFDNN models for FP32, FP16, INT16, and INT8 cases are depicted in Table 9. The parameter count remains identical across all quantization cases since quantization does not alter the architecture of the proposed MIFDNN model for detecting MDs using OCT images. Similarly, we have observed that GFLOPS are constant across all quantization cases, as they depend on the network's layer configuration rather than weight precision. The quantization of the proposed MIFDNN model alters its size, latency, and throughput for real-time detection of MDs using OCT images on an Android device. Due to the smaller size, we have deployed the INT8-based reduced precision MIFDNN model on an Android device for detecting MDs using OCT images. The inference time, throughput, and peak RAM utilization during the inference of the proposed method (U-Net-based denoising and MIFDNN classification) for FP32, FP16, INT16, and INT8 cases are shown in Table 10. It is observed that the throughput of the proposed method on an Android device is high for the INT8 case compared to the FP32, FP16, and INT8 cases for detecting MDs using OCT images. Since the same denoising model has been utilized across all quantization cases, its memory footprint remains relatively stable (574–598 MB in all cases). In contrast, the MIFDNN-based classification model has been quantized using different schemes to highlight their effect on RAM usage. The FP32 of the MIFDNN model has the highest RAM utilization 34.80MB), followed by FP16 and INT16, which exhibit moderate RAM usage (25.90 MB and 24.10 MB), and INT8 achieves the most compact footprint or less RAM utilization (11 MB) for real-time detection of MDs using OCT images.

Figure 6
Grad-CAM plot for (a) the healthy class, (b) the CNV class, (c) the DME class, and (d) the drusen class

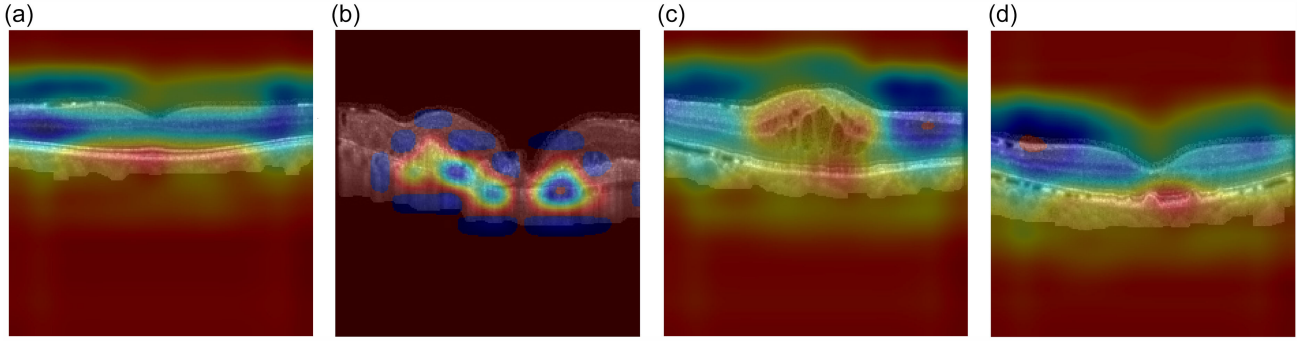

Figure 7
Deployment of the MIFDNN model on an Android device to detect (a) healthy or normal class, (b) CNV class, (c) DME class, and (d) drusen class

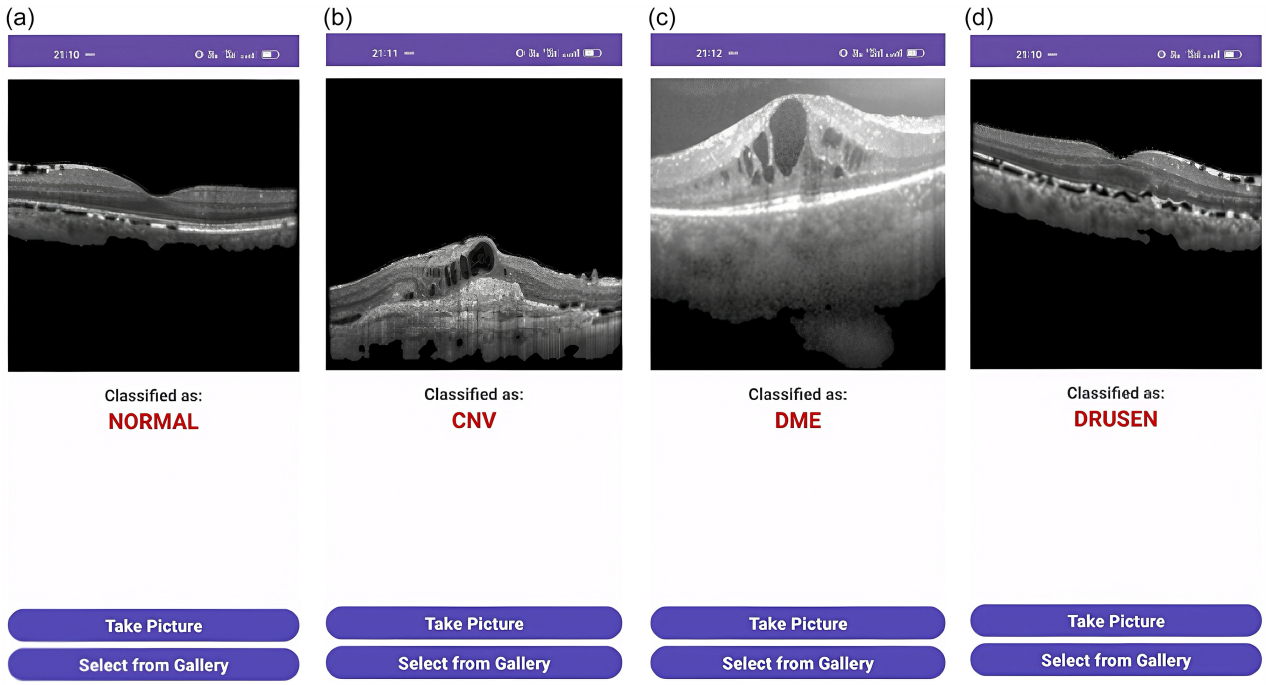

Table 9
Size, parameters, and giga floating point operations per second (GFLOPS) of the MIFDNN model for different quantization cases

Quantization	Model size (KB)	Parameters	GFLOPS
FP32	18535	47,51,812	8.19
FP16	9283	47,51,812	8.19
INT16	18535	47,51,812	8.19
INT8	4748	47,51,812	8.19

We have performed a comparison of the classification performance of the proposed MIFDNN model with various existing methods in Table 11 for detecting MDs using OCT images. The transfer learning-based and attention-based DenseNet models have demonstrated accuracy values lower than 96% for detecting CNV, DME, and drusen classes using OCT images. The iterative fusion-based model with VGG16 as the main branch has obtained an accuracy value of 87.30%. The overall accuracy values of all the reported methods are lower than those of the proposed approach for detecting DME, CNV, and drusen using OCT images. The ViT has approximately 22 million parameters, which is significantly higher than the proposed MIFDNN model for detecting MDs using OCT images. The ViT extracts the global contextual features based on the correlation of patches evaluated from the OCT image [19]. The convolution layers are effective in extracting texture, fine-grained local details, and edge-based features from the OCT image [30]. The proposed MIFDNN consists of convolution layers and feature fusion to effectively extract local features from the OCT image for detecting MDs. Due to this reason, the proposed MIFDNN model has demonstrated higher accuracy than the ViT model in detecting MDs using OCT images. The original IFCNN model has used DL architectures such as VGG16, AlexNet, and GoogleNet [16] as the basic branch for classifying OCT images. The proposed MIFDNN has used a custom-designed basic branch deep CNN architecture to process the OCT image for detecting MDs. The custom deep CNN allows for more effective feature extraction relevant to the MD classification task. The MIFDNN model has achieved an accuracy value of 97.93%, which is 10% higher than the IFCNN model for detecting MDs using OCT images. The deep CNN used in the basic branch module of the proposed MIFDNN model has fewer parameters than the use of the transfer learning-based networks in

Table 10
Resource utilization of the proposed method (U-Net-based denoising and MIFDNN classifier) on an Android device for detecting MDs using OCT images

Quantization	Inference time (sec)	Throughput (images per minute)	Peak RAM usage in MB (U-Net only)	Peak RAM usage in MB (MIFDNN only)	Peak RAM usage in MB (U-Net and MIFDNN)
FP32	2.49	24.09	587.12	33.4	620.52
FP16	2.42	24.79	582.97	25.9	608.87
INT16	2.41	24.89	582.2	24.1	606.3
INT8	0.65	92.3	200.47	10.15	210.62

Table 11
Comparison of MIFDNN model with existing techniques for normal versus CNV versus DME versus drusen classification task using OCT images

Methods developed	Accuracy (%)
HOG features extracted from OCT image and SVM classifier [11]	85.78
VGG16-based transfer learning technique [7]	86.03
InceptionV3-based transfer learning technique [7]	93.01
Iterative fusion based network with VGG16 as in main branch [16]	87.30
Layer-guided CNN model [17]	88.40
Multiscale feature fusion-based DL model [2]	94.57
Deep Multiscale fusion-based DL model [7]	96.03
Vision transformer (ViT) model [19]	95.14
Attention-based DenseNet model [36]	95.83
Class attention transformer (CRAT) [37]	97.83
MIFDNN model (Proposed work)	97.93

the IFCNN model in the inference phase, making the MIFDNN model more suitable for deployment on Android-based devices for the detection of MDs. The PTQ of the MIFDNN model has significantly reduced the size for implementing it on Android-based edge computing applications. The purpose of choosing the Android platform to deploy the proposed method is that it is readily available, cost-effective, and widely accessible on smartphones [9]. The proposed method enables on-device processing of OCT images without depending on the cloud system and can be used in remote or resource-limited environments for detecting MDs. The Android-based on-device processing of the proposed DL method is helpful to enhance the privacy of the patient's OCT image data and make real-time detection of MDs [9].

4.1. Limitations and future scope

The limitations of the proposed method inference on Android devices are the high inference time and lower throughput for the detection of MDs using OCT images. The classification accuracy of the MIFDNN model has been reduced by more than 2% when a cross-dataset based evaluation strategy is used. The federated learning framework [38] can be designed using the proposed hybrid method (U-Net-based denoising and MIFDNN model) with the OCT images of the patients from diverse locations for detecting MDs. The Android-based inference of the proposed method can be used on the client side after obtaining the updated or global model from the server side of the federated learning framework to detect MDs. The implementation of lightweight DL-based models on a field programmable gate array (FPGA)-based low-power embedded system is a challenging research area in medical image processing applications. The FPGA-based embedded healthcare systems have been designed by the researchers in Vinod et al. [9] and Guddati et al. [39] for ultrasound and X-ray image processing applications. In the future, the FPGA implementation-based lightweight versions of DL-based models can be developed for low-power, low-latency, and resource-constrained edge device-based applications to detect MDs using OCT images. In this work, we have used only convolution blocks as feature extractors in the basic branch of the proposed MIFDNN model for detecting MDs using OCT images. The squeeze-and-excitation blocks and attention-enhanced CNN variants [40] can be used in the basic branch of the MIFDNN model to improve feature discriminability for detecting MDs using OCT images.

5. Conclusion

In this paper, an Android-based embedded MIFDNN approach has been proposed for the automated detection of MDs using OCT images. Our approach utilized the U-Net-based model for effective denoising of OCT images, followed by a customized iterative fusion-based DL architecture for detecting MDs. The proposed MIFDNN approach has been utilized in the 3-fold and 5-fold stratified CV strategies, where the 3-fold setup gave the best results, achieving an impressive accuracy of 98.17% for detecting MDs, clearly outperforming previous methods. We applied PTQ (FP16, INT16, INT8), which significantly reduced the model size without compromising performance. The quantized models have been successfully deployed on an Android device and delivered an accuracy value of 98%. Finally, visual tools like t-SNE and Grad-CAM helped validate the proposed MIFDNN model's behavior and interpretability for detecting MDs using OCT images. The proposed approach is suitable for edge computing applications as it has delivered higher classification performance for detecting MDs on an Android device using OCT images.

Ethical Statement

This study does not contain any studies with human or animal subjects performed by any of the authors.

Conflicts of Interest

The authors declare that they have no conflicts of interest to this work.

Data Availability Statement

The data that support the findings of this study are openly available in [Mendeley, Kaggle] at [https://data.mendeley.com/datasets/rscbjbr9sj/3, https://www.kaggle.com/datasets/obulisainaren/retinal-oct-c8].

Author Contribution Statement

Umar Shafiq Ahmad: Methodology, Software, Validation, Formal analysis, Investigation, Resources, Data curation, Writing – original draft. **Rajesh Kumar Tripathy:** Conceptualization, Writing – review & editing, Visualization, Supervision, Project administration.

References

[1] Zhou, C., Li, S., Ye, L., Chen, C., Liu, S., Yang, H., . . . , & Xu, X. (2023). Visual impairment and blindness caused by retinal diseases: A nationwide register-based study. *Journal of Global Health*, *13*, 04126. https://doi.org/10.7189/jogh.13.04126

[2] Das, V., Dandapat, S., & Bora, P. K. (2019). Multi-scale deep feature fusion for automated classification of macular pathologies from OCT images. *Biomedical Signal Processing and Control*, *54*, 101605. https://doi.org/10.1016/j.bspc.2019.101605

[3] Servillo, A., Scandale, P., Oldoni, G., Begar, P. G., Bandello, F., Miserocchi, E., & Cicinelli, M. V. (2025). Inflammatory choroidal neovascularization: An evidence-based update.

Survey of Ophthalmology, *70*(3), 451–466. https://doi.org/10.1016/j.survophthal.2024.12.004

[4] Vujosevic, S., Lupidi, M., Donati, S., Astarita, C., Gallinaro, V., & Pilotto, E. (2024). Role of inflammation in diabetic macular edema and neovascular age-related macular degeneration. *Survey of Ophthalmology*, *69*(6), 870–881. https://doi.org/10.1016/j.survophthal.2024.07.006

[5] Mukriyani, H., Malmqvist, L., Subhi, Y., & Hamann, S. (2024). Prevalence of optic disc drusen: A systematic review, meta-analysis and forecasting study. *Acta Ophthalmologica*, *102*(1), 15–24. https://doi.org/10.1111/aos.15690

[6] Chua, J., Tan, B., Wong, D., Garhöfer, G., Liew, X. W., Popa-Cherecheanu, A., . . . , & Schmetterer, L. (2024). Optical coherence tomography angiography of the retina and choroid in systemic diseases. *Progress in Retinal and Eye Research*, *103*, 101292. https://doi.org/10.1016/j.preteyeres.2024.101292

[7] Das, V., Dandapat, S., & Bora, P. K. (2021). Automated classification of retinal OCT images using a deep multi-scale fusion CNN. *IEEE Sensors Journal*, *21*(20), 23256–23265. https://doi.org/10.1109/JSEN.2021.3108642

[8] Makhijani, P., Nath, A., Vakani, H., Mistry, M., Koradiya, H., Jayswal, H. S., . . . , & Dubey, N. (2025). Lime diseases classification using machine learning and spectrometry. In *Information Systems for Intelligent Systems*, *1*, 405–414. https://doi.org/10.1007/978-981-96-1206-2_31

[9] Vinod, A., Guddati, P., Kumar Panda, A., & Kumar Tripathy, R. (2024). A lightweight deep convolutional neural network implemented on FPGA and Android devices for detection of breast cancer using ultrasound images. *IEEE Access*, *12*, 179190–179203. https://doi.org/10.1109/ACCESS.2024.3506334

[10] Akpinar, M. H., Sengur, A., Faust, O., Tong, L., Molinari, F., & Acharya, U. R. (2024). Artificial intelligence in retinal screening using OCT images: A review of the last decade (2013–2023). *Computer Methods and Programs in Biomedicine*, *254*, 108253. https://doi.org/10.1016/j.cmpb.2024.108253

[11] Srinivasan, P. P., Kim, L. A., Mettu, P. S., Cousins, S. W., Comer, G. M., Izatt, J. A., & Farsiu, S. (2014). Fully automated detection of diabetic macular edema and dry age-related macular degeneration from optical coherence tomography images. *Biomedical Optics Express*, *5*(10), 3568–3577. https://doi.org/10.1364/BOE.5.003568

[12] Lemaître, G., Rastgoo, M., Massich, J., Cheung, C. Y., Wong, T. Y., Lamoureux, E., . . . , & Sidibé, D. (2016). Classification of SD-OCT volumes using local binary patterns: Experimental validation for DME detection. *Journal of Ophthalmology*, *2016*(1), 3298606. https://doi.org/10.1155/2016/3298606

[13] Albarrak, A., Coenen, F., & Zheng, Y. (2013). Age-related macular degeneration identification in volumetric optical coherence tomography using decomposition and local feature extraction. In *Proceedings of 2013 International Conference on Medical Image, Understanding and Analysis*, 59–64.

[14] Simonyan, K., & Zisserman, A. (2015). Very deep convolutional networks for large-scale image recognition. *arXiv Preprint: 1409.1556*.

[15] Szegedy, C., Vanhoucke, V., Ioffe, S., Shlens, J., & Wojna, Z. (2016). Rethinking the inception architecture for computer vision. In *2016 IEEE Conference on Computer Vision and Pattern Recognition*, 2818–2826. https://doi.org/10.1109/CVPR.2016.308

[16] Fang, L., Jin, Y., Huang, L., Guo, S., Zhao, G., & Chen, X. (2019). Iterative fusion convolutional neural networks for classification of optical coherence tomography images. *Journal of Visual Communication and Image Representation*, *59*, 327–333. https://doi.org/10.1016/j.jvcir.2019.01.022

[17] Huang, L., He, X., Fang, L., Rabbani, H., & Chen, X. (2019). Automatic classification of retinal optical coherence tomography images with layer guided convolutional neural network. *IEEE Signal Processing Letters*, *26*(7), 1026–1030. https://doi.org/10.1109/LSP.2019.2917779

[18] Mishra, S. S., Mandal, B., & Puhan, N. B. (2022). Perturbed composite attention model for macular optical coherence tomography image classification. *IEEE Transactions on Artificial Intelligence*, *3*(4), 625–635. https://doi.org/10.1109/TAI.2021.3135797

[19] Akça, S., Garip, Z., Ekinci, E., & Atban, F. (2024). Automated classification of choroidal neovascularization, diabetic macular edema, and drusen from retinal OCT images using vision transformers: A comparative study. *Lasers in Medical Science*, *39*(1), 140. https://doi.org/10.1007/s10103-024-04089-w

[20] Jaimes, W. J., Arenas, W. J., Navarro, H. J., & Altuve, M. (2025). Detection of retinal diseases from OCT images using a VGG16 and transfer learning. *Discover Applied Sciences*, *7*(3), 160. https://doi.org/10.1007/s42452-025-06565-6

[21] Bhandari, M., Shahi, T. B., & Neupane, A. (2023). Evaluating retinal disease diagnosis with an interpretable lightweight CNN model resistant to adversarial attacks. *Journal of Imaging*, *9*(10), 219. https://doi.org/10.3390/jimaging9100219

[22] Altaf, A., & Tripathy, R. K. (2025). An IoT-enabled deep learning approach implemented on Android device for automated identification of breast cancer using thermal images. *Smart Wearable Technology*, *1*, A4. https://doi.org/10.47852/bonviewSWT52025252

[23] Kermany, D. (2018). *Labeled optical coherence tomography (OCT) and chest X-ray images for classification* [Dataset]. *Mendeley Data*. https://doi.org/10.17632/RSCBJBR9SJ.2

[24] Kermany, D. S., Goldbaum, M., Cai, W., Valentim, C. C. S., Liang, H., Baxter, S. L., . . . , & Zhang, K. (2018). Identifying medical diagnoses and treatable diseases by image-based deep learning. *Cell*, *172*(5), 1122–1131. https://doi.org/10.1016/j.cell.2018.02.010

[25] Naren, O. S. (2021). *Retinal OCT image classification—C8* [Dataset]. *Kaggle*. https://doi.org/10.34740/KAGGLE/DSV/2736749

[26] Ronneberger, O., Fischer, P., & Brox, T. (2015). U-Net: Convolutional networks for biomedical image segmentation. In *Medical Image Computing and Computer-Assisted Intervention: 18th International Conference*, 234–241. https://doi.org/10.1007/978-3-319-24574-4_28

[27] Kim, J., & Tran, L. (2020). Ensemble learning based on convolutional neural networks for the classification of retinal diseases from optical coherence tomography images. In *2020 IEEE 33rd International Symposium on Computer-Based Medical Systems*, 532–537. https://doi.org/10.1109/CBMS49503.2020.00106

[28] Cuevas, E., & Rodríguez, A. N. (2024). *Image processing and machine learning: Advanced topics in image analysis and machine learning* (Vol. *2*). USA: CRC Press. https://doi.org/10.1201/9781032662466

[29] Chen, K., Xuan, Y., Lin, A., & Guo, S. (2021). Lung computed tomography image segmentation based on U-Net network fused with dilated convolution. *Computer Methods and Programs in Biomedicine*, *207*, 106170. https://doi.org/10.1016/j.cmpb.2021.106170

[30] Wani, M. A., Sultan, B., Ali, S., & Sofi, M. A. (2025). *Advances in deep learning*, Vol. *2*. Singapore: Springer. https://doi.org/10.1007/978-981-96-3498-9

[31] Polat, G., Çağlar, Ü. M., & Temizel, A. (2025). Class distance weighted cross entropy loss for classification of disease severity. *Expert Systems with Applications*, *269*, 126372. https://doi.org/10.1016/j.eswa.2024.126372

[32] Karhade, J., Dash, S., Ghosh, S. K., Dash, D. K., & Tripathy, R. K. (2022). Time–frequency-domain deep learning framework for the automated detection of heart valve disorders using PCG signals. *IEEE Transactions on Instrumentation and Measurement*, *71*, 2506311. https://doi.org/10.1109/TIM.2022.3163156

[33] Wei, L., Ma, Z., Yang, C., & Yao, Q. (2024). Advances in the neural network quantization: A comprehensive review. *Applied Sciences*, *14*(17), 7445. https://doi.org/10.3390/app14177445

[34] Huang, A. A., & Huang, S. Y. (2023). Computation of the distribution of model accuracy statistics in machine learning: Comparison between analytically derived distributions and simulation-based methods. *Health Science Reports*, *6*(4), e1214. https://doi.org/10.1002/hsr2.1214

[35] Pembury Smith, M. Q. R., & Ruxton, G. D. (2020). Effective use of the McNemar test. *Behavioral Ecology and Sociobiology*, *74*(11), 133. https://doi.org/10.1007/s00265-020-02916-y

[36] Talaat, F. M., Ali, A. A. A., ElGendy, R., & ELShafie, M. A. (2025). Deep attention for enhanced OCT image analysis in clinical retinal diagnosis. *Neural Computing and Applications*, *37*(2), 1105–1125. https://doi.org/10.1007/s00521-024-10450-5

[37] Yang, M., Du, J., & Lv, R. (2025). CRAT: Advanced transformer-based deep learning algorithms in OCT image classification. *Biomedical Signal Processing and Control*, *104*, 107544. https://doi.org/10.1016/j.bspc.2025.107544

[38] Li, M., Xu, P., Hu, J., Tang, Z., & Yang, G. (2025). From challenges and pitfalls to recommendations and opportunities: Implementing federated learning in healthcare. *Medical Image Analysis*, *101*, 103497. https://doi.org/10.1016/j.media.2025.103497

[39] Guddati, P., Dash, S., & Tripathy, R. K. (2024). FPGA implementation of the proposed DCNN model for detection of tuberculosis and pneumonia using CXR images. *IEEE Embedded Systems Letters*, *16*(4), 445–448. https://doi.org/10.1109/LES.2024.3370833

[40] Nath, A., Roy, O., Silveri, P., & Patel, S. (2025). Deep learning approach with ConvNeXt-SE-attn model for in vitro oral squamous cell carcinoma and chemotherapy analysis. *MethodsX*, *15*, 10s3519. https://doi.org/10.1016/j.mex.2025.103519

How to Cite: Ahmad, U. S., & Tripathy, R. K. (2025). An Android-Based Embedded Modified Iterative Fusion Deep Neural Network for Automated Detection of Macular Diseases Using OCT Images. *Smart Wearable Technology*. https://doi.org/10.47852/bonviewSWT52026773